Analytical model of light reflectance for extraction of the optical properties in small volumes of turbid media

Roberto Reif,[1,*] Ousama A'Amar,[1] and Irving J. Bigio[1,2]

[1]Department of Biomedical Engineering, Boston University, 44 Cummington Street, 4th Floor, Boston, Massachusetts 02215, USA

[2]Department of Electrical and Computer Engineering, Boston University, 44 Cummington Street, 4th Floor, Boston, Massachusetts 02215, USA

*Corresponding author: robreif@bu.edu

Received 9 April 2007; revised 4 August 2007; accepted 22 August 2007; posted 23 August 2007 (Doc. ID 81960); published 9 October 2007

Monte Carlo simulations and experiments in tissue phantoms were used to empirically develop an analytical model that characterizes the reflectance spectrum in a turbid medium. The model extracts the optical properties (scattering and absorption coefficients) of the medium at small source-detector separations, for which the diffusion approximation is not valid. The accuracy of the model and the inversion algorithm were investigated and validated. Four fiber probe configurations were tested for which both the source and the detector fibers were tilted at a predetermined angle, with the fibers parallel to each other. This parallel-fiber geometry facilitates clinical endoscopic applications and ease of fabrication. Accurate extraction of tissue optical properties from *in vivo* spectral measurements could have potential applications in detecting, noninvasively and in real time, epithelial (pre)cancers.

OCIS codes: 170.3660, 170.3890, 170.4580, 170.6510, 170.7050.

1. Introduction

An important challenge in biomedical research is to noninvasively characterize tissue conditions, for the purposes of diagnosis of disease, such as (pre)cancerous conditions, or for monitoring response to treatment. *In situ* measurements of the optical properties of tissue may reveal information concerning the morphological and biochemical composition of the tissue. Optical techniques are currently being used *in vivo* to identify changes that occur in biological tissues [1–3] associated with disease progression.

Tissues can be characterized by their optical properties, which are defined by the absorption coefficient (μ_a), the scattering coefficient (μ_s), the phase function [$p(\theta)$], the anisotropy value ($g = \langle \cos\theta \rangle$) and the reduced scattering coefficient [$\mu_s' = \mu_s(1 - g)$]. The diffusion approximation to the Boltzman transport equation is a method that has been used successfully to determine the absorption coefficient and the reduced scattering coefficient in turbid media [4–6]. The validity of the diffusion approximation is limited to media with higher scattering than absorption ($\mu_s' \gg \mu_a$), which is satisfied in biological tissues for the wavelength region between 600–900 nm, and to large separations between the source and the detector ($\rho \gg 1/\mu_s'$). As a consequence, the collected photons travel through a large volume of tissue, and the extracted optical properties represent average values for the tissue volume probed. However, many clinical settings require small fiber probes (e.g., endoscope working channels typically have a diameter of <3 mm). Different methods have been used to determine the optical properties in turbid media at small source-detector separations [7–19], including some based on the diffusion approximation [20,21]. Various fiber optic probe designs have been developed for reflectance and fluorescence measurements [22–25]. In many applications the tissues of interest are thin. Most cancers arise in the epithelium, which is a superficial tissue layer with a thickness, typically, of 100–500 μm. Hence, sensitivity to the optical properties of the epithelial layer requires superficial mea-

0003-6935/07/297317-12$15.00/0

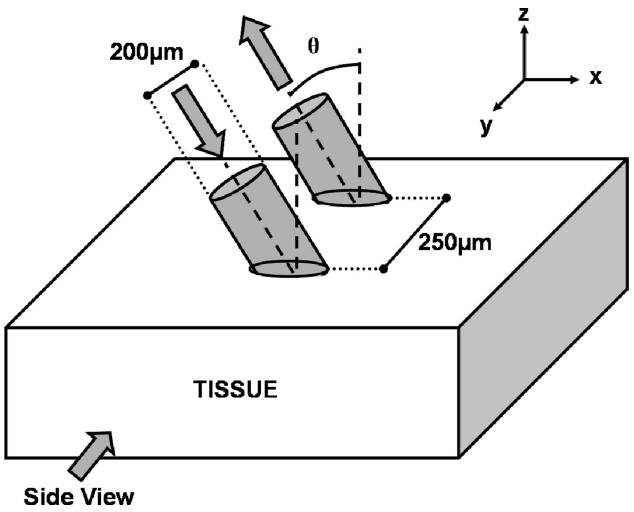

Fig. 1. Diagram of the fiber probe design used in both Monte Carlo simulations and experiments in tissue phantoms.

surement techniques. The penetration depth of the collected photons depends on the fiber probe geometry and the optical properties of the sample [16,24,26,27], which may allow the interrogation depth to extend beyond the epithelial layer.

Tilted fiber optic probes have been employed for controlling the depth of penetration in tissue spectroscopy applications [26–30]. We put forward the use of a new probe design for which the source and the detector fibers are tilted with respect to the tissue surface but, unlike previously published designs, the fibers are kept parallel to each other as observed in Fig. 1. This type of fiber probe geometry offers the benefits of convenience for clinical applications with endoscopes, and ease of fabrication. Further, we propose an innovative and simple analytical model that can extract the absorption and scattering coefficients of a turbid medium using a small source-detector separation, based on a simple analysis of the reflectance spectrum. The objective is to develop a diagnostic tool that would facilitate the determination of biologically relevant parameters such as size and size distribution of cellular organelles, tissue blood content, and hemoglobin oxygen saturation. The model is developed and validated using Monte Carlo (MC) simulations and experiments with tissue phantoms.

2. Materials and Methods

A. Monte Carlo Simulations

A MC code that simulates light transport within a scattering and absorbing medium has been developed based on previous codes [31,32], using a variance reduction technique [33]. The MC code simulates a probe that comprises two fibers (a source and a detector), as depicted in Fig. 1. Each fiber has a core diameter of 200 μm and a numerical aperture (NA) of 0.22 in air. The fibers have a center-to-center separation of 250 μm. Both fibers can be tilted at an angle (θ) relative to the tissue surface normal, in the x–z plane, such that the fibers are parallel to each other. Four tilt angles have been investigated: 0°, 15°, 30°, and 45°. The surfaces of the fibers were modeled to be polished at an angle such that the faces of the fibers were parallel to the surface of the medium. Thus, the faces of the fibers had a circular or elliptical shape depending on whether $\theta = 0$ or $\theta > 0$, respectively. Photons were launched from points within the surface of the source fiber into the medium, with an angle within the NA and appropriate tilt angle of the fiber (including index mismatch correction). The launch point and angle of each photon were chosen by using a random uniform distribution. The propagation of the photons within the medium was determined by the absorption coefficient, the scattering coefficient, and the Henyey–Greenstein (HG) [34] or modified Henyey–Greenstein (MHG) [9,35] phase function. Unless otherwise indicated, throughout this paper we will be referring to the HG phase function. Photons were terminated from the simulation when they had traveled farther than a specified distance from the source fiber, had a path length larger than a specified value, or had left the surface of the medium. The specified distance and path-length values were selected such that they had a negligible effect on the results of the simulation. The simulation also accounts for reflection at the surface of the medium due to the mismatch of the index of refraction. Photons were collected when they arrived at the surface of the medium within the diameter, NA, and tilt angle of the collection fiber. The index of refraction of the fibers and the medium were set to 1.5 and 1.4, respectively. Over 2×10^6 photons were tracked per simulation.

The paths of photons traveling from a source to a detector fiber depend on the optical properties of the medium and on the fiber probe geometry. When the fibers are tilted at an angle θ_f, the light is bent inside the medium to an angle θ_m, which is described by Snell's law ($n_f \sin \theta_f = n_m \sin \theta_m$), where n_f and n_m are the indices of refraction of the fiber and the medium, respectively. Since the index of the fiber is typically higher than the index of the medium, then $\theta_m > \theta_f$. Figure 2 depicts the normalized voxel visitation history of the collected photons from a side view (as indicated in Fig. 1) for the 0° and 45° fiber probe configurations in a medium with $\mu_a = 0.1\ \text{cm}^{-1}$, μ_s'

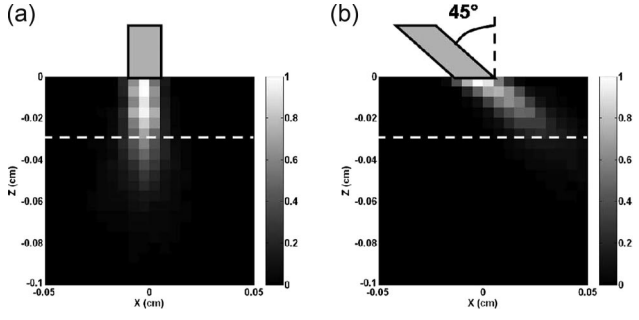

Fig. 2. Normalized voxel visitation history of Monte Carlo simulations for the (a) 0° and (b) 45° fiber probe configuration. The dotted line depicts a depth of 300 μm.

$= 10\ \mathrm{cm}^{-1}$, and $g = 0.9$. The dotted white line represents a depth of 300 μm. It is observed that the 45° fiber probe configuration is more sensitive to collecting light in superficial volumes of tissue, compared to the 0° fiber probe configuration. It is important to note that the depth of penetration of the collected photons is also dependent on the optical properties of the tissue.

B. Instrumentation

The experimental setup for the reflectance measurements consisted on a pulsed Xenon-arc lamp (LS-1130-3, Perkin Elmer) as a broadband light source, a spectrometer (S2000, Ocean Optics, Inc.) and a fiber probe for the delivery and collection of the light to and from the sample. Four fiber probe configurations were fabricated with tilt angles of 0°, 15°, 30°, and 45°, as depicted in Fig. 1. The probes had two multimode optical fibers (source and detector), which are parallel to each other. The center-to-center separation between the fibers was approximately 250 μm. Each optical fiber had a core diameter of 200 μm and a NA of 0.22 in air. The tips of the probes were polished parallel to the surface of the medium for each of the angles.

The tilt angles of the fiber probes were verified by inserting the angled tip in a dilute solution of titanium dioxide and water, and measuring the output angle of a HeNe (632.8 nm) laser. Snell's law was used to determine that the probes were within 1.5° of the expected tilt angle.

C. Liquid Tissue Phantoms

Liquid tissue phantoms were prepared using deionized water, Intralipid-10% (Fresenius Kabi) as a source of scattering and Indigo Blue dye (Daler-Rowney) as an absorber. Intralipid-10% has been previously demonstrated to scatter light preferentially in the forward direction [36]. The wavelength-dependent extinction coefficient of the Indigo Blue dye was measured using a spectrophotometer (Varian, Cary-50), and the absorption spectrum, normalized to the peak at 610 nm, is shown in Fig. 3. The reduced scattering coefficients of the tissue phantoms were determined using a method of spatially dependent diffuse reflectance spectroscopy [37]. Known amounts of dye were added to the phantom to obtain the appropriate absorption coefficient. It is important to note that the amount of dye solution added did not exceed 0.5% of the volume of the phantom; therefore, the alterations of the scattering properties were negligible. Unless otherwise indicated, the values of the reduced scattering coefficient and absorption coefficient discussed in this paper are at a wavelength of 610 nm. Each phantom contained 200 ml of solution and was placed inside a cylindrical container.

D. Calibration Phantom

A calibration liquid phantom was made by suspending 0.16 grams of titanium dioxide powder (J. T. Baker) in 200 ml of deionized water. Titanium dioxide has an anisotropy value of ~0.5 in aqueous suspension [38]. No absorber was added to the calibration phantom. The reduced scattering coefficient of the calibration phantom was determined using the method of spatially dependent diffuse reflectance spectroscopy [37].

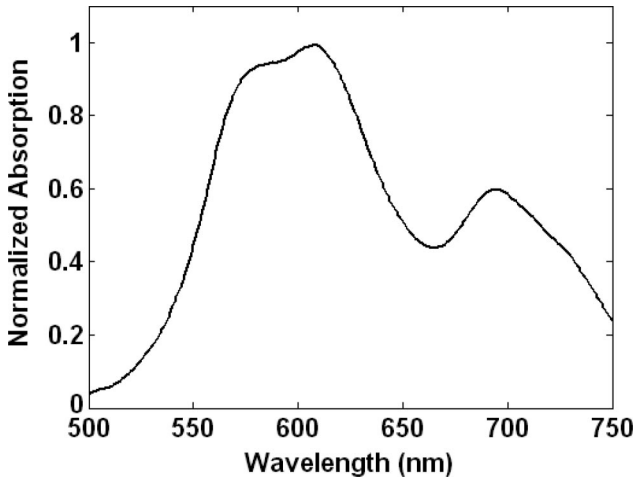

Fig. 3. Absorption spectrum of Indigo Blue dye normalized to the peak at 610 nm.

E. Data Acquisition

Spectral measurements were obtained by subtracting a dark measurement (lamp was not fired) from a light measurement (lamp was fired). Averages of 15 measurements were taken for each spectrum. Reflectance values were calculated by dividing each spectrum by the spectrum obtained with the calibration phantom. The integration time of the spectrometer was the same for the measurements taken by both the tissue and the calibration phantoms, and it was varied between 8 and 60 ms such that the signal to noise ratio was at least 25:1.

The measurements were taken by inserting the fiber probe into the liquid phantoms. The diameter of the fiber probe housing was large enough (3 mm) compared to the fiber separation (250 μm), such that there was no difference between measurements taken at the surface of the phantom or submerging the probe inside the sample. The end of the fiber probe was located more than 1 cm from the bottom and walls of the container to avoid interference from the boundaries.

3. Results

A. Reflectance as a Function of the Reduced Scattering Coefficient

For the development of the model, the reflectance from a medium that scatters light was analyzed for conditions with very little absorption ($\mu_a \leq 0.01\ \mathrm{cm}^{-1}$). MC simulations were run for a medium with an absorption coefficient of $0.01\ \mathrm{cm}^{-1}$ and for five values of reduced scattering coefficient ($\mu_s' = 5$, 10, 15, 20, and $25\ \mathrm{cm}^{-1}$). The anisotropy value was set to 0.9. Four different fiber tilt angles were modeled

($\theta = 0°$, 15°, 30°, and 45°). The absolute reflectance (R^{ABS}), is defined as the ratio of the collected light (I) over the incident light (I_0), and is calculated using Eq. (1):

$$R^{ABS} = \frac{I}{I_0} = \frac{\sum_{i=1}^{TPC} \exp(-\mu_a l_i)}{TPL}, \quad (1)$$

where TPC is the total number of photons collected, TPL is the total number of photons launched, μ_a is the absorption coefficient, and l_i is the path length of each collected photon. To analyze the reflectance experimentally, eight tissue phantoms were prepared with different concentrations of Intralipid-10% in deionized water. No dye was added; therefore the absorption coefficient was assumed to be negligible for the spectral range studied. The resulting reduced scattering coefficients of the tissue phantoms varied between 3 and 20 cm^{-1}. Measurements were taken on each phantom with each of the four fiber optic probe configurations. It is difficult to determine experimentally the absolute value of the incident light; however, a relative value of the incident light can be obtained by measuring the collected light from a calibration phantom. The relative reflectance of a phantom [$R_P^{REL}(\lambda)$] has been defined as the ratio of the absolute reflectance of a phantom [$R_P^{ABS}(\lambda)$] over the absolute reflectance of a calibration phantom [$R_C^{ABS}(\lambda_0)$]. Throughout this paper, $R_C^{ABS}(\lambda_0)$ represents the absolute reflectance of the calibration phantom at $\lambda_0 = 610$ nm, which will be a constant given that we always use the same calibration phantom and wavelength. If the incident light of the reflectance measurements in the tissue and calibration phantom is the same [$I_0(\lambda) = I_0(\lambda_0)$], the expression for the relative reflectance will be independent of the incident light, as described in Eq. (2).

$$R_P^{REL}(\lambda) = \frac{R_P^{ABS}(\lambda)}{R_C^{ABS}(\lambda_0)} = \frac{I_P(\lambda)}{I_0(\lambda)} \frac{I_0(\lambda_0)}{I_C(\lambda_0)} = \frac{I_P(\lambda)}{I_C(\lambda_0)}, \quad (2)$$

where $I_P(\lambda)$ is the collected light from the tissue phantom and $I_C(\lambda_0)$ is the collected light from the calibration phantom at 610 nm. Note that since $R_C^{ABS}(\lambda_0)$ is a constant, $R_P^{REL}(\lambda)$ is linearly proportional to $R_P^{ABS}(\lambda)$.

The relative reflectance of the tissue phantoms were calculated, at the wavelength of 610 nm, as the ratio of the tissue phantom measurement over the measurement obtained with the calibration phantom. The incident light on the tissue and calibration phantom was the same.

The reflectance as a function of the reduced scattering coefficient, using the 45° fiber probe configuration, obtained with MC simulations and experiments in tissue phantoms is shown in Figs. 4(a) and 4(b), respectively. It is observed that there is a linear relationship between the reduced scattering coefficient and the reflectance. Equation (3) is a straight-line fit to the data using linear least squares, where $R(0)$ is the reflectance when there is negligible absorption.

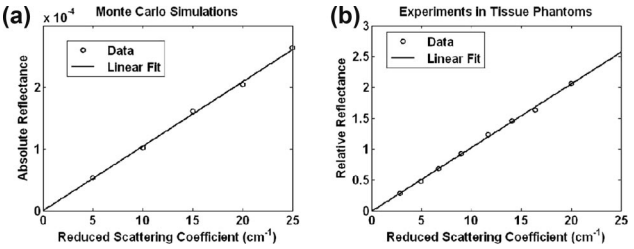

Fig. 4. Reflectance as a function of the reduced scattering coefficient for the 45° fiber probe configuration in a nonabsorbing medium obtained with (a) Monte Carlo simulations and (b) experiments in tissue phantoms.

$$R(0) = a\mu_s' + a_0. \quad (3)$$

Similar results were obtained with the 0°, 15°, and 30° fiber probe configurations (data not shown).

The determined values of the coefficients a and a_0 are presented in Table 1. The reason that the values obtained with MC simulations and experiments in tissue phantoms differ is because MC simulations determine absolute reflectance values, and the experiments determine relative reflectance values (i.e., we did not attempt to measure the precise amount of light emitted by the source fiber). The value of a_0 is a function of the anisotropy value and phase function of the scattering centers, as it will be discussed in Subsection 3.C.

B. Reflectance as a Function of the Reduced Scattering and Absorption Coefficient

To further develop the model, the reflectance was analyzed for conditions where the tissue phantom both scatters and absorbs light. MC simulations were run for a medium with 19 values of absorption coefficient ($\mu_a = 0.1$ to 10 cm^{-1}) and for three values of reduced scattering coefficient ($\mu_s' = 5$, 10, and 20 cm^{-1}). The anisotropy value was set to 0.9. Four different tilt angles were modeled ($\theta = 0°$, 15°, 30°, and 45°). The absolute reflectance was calculated using Eq. (1).

For the experiments, liquid tissue phantoms were prepared with three values of reduced scattering coefficient ($\mu_s' = 5.5$, 10.6, and 20.7 cm^{-1}) and 19 values of absorption coefficient ($\mu_a = 0.12$ to 8 cm^{-1}). The values of the optical properties, quoted at 610 nm, were selected based on the range of values commonly found in tissue [39]. Measurements were taken on each phantom with each of the four fiber optic probe

Table 1. Values for the Coefficients a and a_0 Obtained With Monte Carlo Simulations and Experiments in Tissue Phantoms With a 0°, 15°, 30°, and 45° Fiber Probe Configuration

		Fiber Tilt Angle			
		0°	15°	30°	45°
a	MC	1.2×10^{-5}	1.1×10^{-5}	1.1×10^{-5}	1.0×10^{-5}
	Experiment	0.11	0.11	0.11	0.10
a_0	MC	0.0×10^{-5}	0.0×10^{-5}	0.0×10^{-5}	0.0×10^{-5}
	Experiment	−0.04	−0.04	−0.03	−0.01

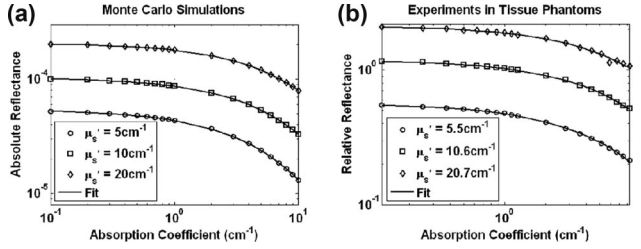

Fig. 5. Reflectance as a function of the absorption coefficient for the 45° fiber probe configuration obtained with (a) Monte Carlo simulations and (b) experiments in tissue phantoms.

configurations. The relative reflectance was calculated at the wavelength of 610 nm by dividing the tissue phantom measurements by the measurements obtained with the calibration phantom.

The reflectance as a function of the absorption coefficient for several reduced scattering coefficient values, using the 45° fiber probe configuration, obtained with MC simulations and experiments in tissue phantoms is presented in Figs. 5(a) and 5(b), respectively. Similar results were obtained with the 0°, 15°, and 30° fiber probe configurations (data not shown).

From the previous section, it was determined that the reflectance is linearly proportional to the reduced scattering coefficient when there is negligible absorption. Beer's law states that the intensity should decay exponentially as a function of the absorption coefficient; therefore, we expand the model using Eq. (4):

$$R(\mu_a) = R(0)\exp(-\mu_a\langle L\rangle), \tag{4}$$

where $R(0)$ is given by Eq. (3), and $\langle L\rangle$ is the "mean average path length" of the collected photons, as defined in [40].

The mean average path length of the collected photons can be described as being inversely proportional to both the scattering and absorption properties of the medium, for small source-detector separations. For that geometry, the collected photons from a highly scattering medium reverse their direction close to the surface of the tissue and travel a short path. Conversely the photons collected from a low-scattering medium penetrate a longer distance into the medium before scattering and reversing their directions. The mean average path length of the collected photons is also longer in a low-absorption medium than in a high-absorbing medium because the probability for a collected photon to travel a long path is reduced for the latter case. The model for the mean average path length is given by Eq. (5):

$$\langle L\rangle = \frac{b}{(\mu_a\mu_s')^c}, \tag{5}$$

where b and c are fitting coefficients. Equation (6) is obtained by combining Eqs. (3), (4), and (5).

$$R(\mu_a) = (a\mu_s' + a_0)\exp\left(-\mu_a\frac{b}{(\mu_a\mu_s')^c}\right). \tag{6}$$

Table 2. Values for the Coefficient *b* Obtained With Monte Carlo Simulations and Experiments in Tissue Phantoms With a 0°, 15°, 30°, and 45° Fiber Probe Configuration

	Fiber Tilt Angle			
	0°	15°	30°	45°
MC				
$\mu s' = 5$	0.33	0.32	0.32	0.32
$\mu s' = 10$	0.33	0.31	0.31	0.29
$\mu s' = 20$	0.30	0.30	0.30	0.28
Mean	**0.32**	**0.31**	**0.31**	**0.30**
Experiment				
$\mu s' = 5.5$	0.20	0.26	0.25	0.26
$\mu s' = 10.6$	0.22	0.25	0.25	0.25
$\mu s' = 20.7$	0.23	0.25	0.23	0.24
Mean	**0.22**	**0.25**	**0.24**	**0.25**

Equation (6) was used to provide the fit to the reflectance measurements shown in Fig. 5, for which a, a_0, μ_a, and μ_s' were known, and the values of b and c were determined (Tables 2 and 3). It is noted that for a given tilt-angle fiber probe, the values of b and c agree well for the three different reduced scattering coefficients, which helps to validate the model. The values of b differ between the MC simulations and the experiments, while the values of c agree well.

We repeated the MC simulations with the same conditions described in Subsections 3.A and 3.B but the indices of refraction of the fiber (n_f) and medium (n_m) were set to 1.46 and 1.33, respectively. The simulations were run only for the 0° and 45° fiber probe. The value of the coefficients a and a_0 and the mean value of the coefficients b and c are listed in Table 4 under column B. The values of the coefficients obtained with MC simulations in Tables 1, 2, and 3 are listed in Table 4 under column A. As a result, the values of the coefficients do not depend on the indices of refraction of the fiber and medium.

We also repeated the MC simulations with the same conditions described in Subsections 3.A and 3.B but with the center-to-center fiber separation set to 200 μm. The simulations were only run for the 0° and

Table 3. Values for the Coefficient *c* Obtained With Monte Carlo Simulations and Experiments in Tissue Phantoms With a 0°, 15°, 30°, and 45° Fiber Probe Configuration

	Fiber Tilt Angle			
	0°	15°	30°	45°
MC				
$\mu s' = 5$	0.21	0.21	0.21	0.20
$\mu s' = 10$	0.21	0.22	0.21	0.19
$\mu s' = 20$	0.20	0.20	0.20	0.19
Mean	**0.21**	**0.21**	**0.21**	**0.19**
Experiment				
$\mu s' = 5.5$	0.20	0.20	0.20	0.20
$\mu s' = 10.6$	0.20	0.20	0.20	0.20
$\mu s' = 20.7$	0.20	0.20	0.20	0.20
Mean	**0.20**	**0.20**	**0.20**	**0.20**

Table 4. Values for the Coefficients a, a_0 b, and c Obtained With Monte Carlo Simulations With the 0° and 45° Fiber Probe Configuration Under Different Conditions[a]

	A	B	C	D	E	F	G	H
Parameters								
n_f	1.5	**1.46**	1.5	1.5	1.5	1.5	1.5	1.5
n_m	1.4	**1.33**	1.4	1.4	1.4	1.4	1.4	1.4
Separation (μm)	250	250	**200**	250	250	250	250	250
Phase function	HG	HG	HG	**MHG**	HG	HG	HG	HG
g	0.9	0.9	0.9	0.9	**0.2**	**0.5**	**0.75**	**0.95**
Tilt angle								
0°								
a	1.2×10^{-5}	1.2×10^{-5}	1.4×10^{-5}	1.2×10^{-5}	1.1×10^{-5}	1.1×10^{-5}	1.2×10^{-5}	1.2×10^{-5}
a_0	0.0×10^{-5}	0.0×10^{-5}	0.0×10^{-5}	1.5×10^{-5}	4.8×10^{-5}	1.7×10^{-5}	0.0×10^{-5}	0.0×10^{-5}
b	0.32	0.30	0.26	0.31	0.36	0.32	0.31	0.31
c	0.21	0.21	0.21	0.21	0.20	0.20	0.20	0.19
45°								
a	1.0×10^{-5}	1.1×10^{-5}	1.3×10^{-5}	1.0×10^{-5}	9.9×10^{-5}	1.0×10^{-5}	1.1×10^{-5}	1.0×10^{-5}
a_0	0.0×10^{-5}	0.0×10^{-5}	0.0×10^{-5}	2.1×10^{-5}	4.0×10^{-5}	2.0×10^{-5}	0.0×10^{-5}	0.0×10^{-5}
b	0.30	0.30	0.25	0.30	0.35	0.32	0.30	0.30
c	0.19	0.20	0.20	0.20	0.20	0.21	0.21	0.21

[a]Bold indicates the changes in the parameters referenced to the parameters described in column A. See text for details.

45° fiber probe. The values of the coefficients a and a_0 and the mean value of the coefficients b and c are listed in Table 4 under column C. The values of a and b depend on the center-to-center separation of the fibers.

Finally, we reanalyzed the same experimental data described in Subsections 3.A and 3.B, but we used a calibration phantom prepared with deionized water and Intralipid. The values of a obtained for the 0°, 15°, 30°, and 45° fibers were 0.19, 0.18, 0.18, and 0.18, respectively, and the values for a_0 were −0.06, −0.06, −0.05, and −0.02, respectively. The values of the coefficients b and c were exactly the same as the values listed in Tables 2 and 3, indicating that the calibration phantom only affects the coefficients a and a_0 in a linear manner. The fact that only the coefficients a and a_0 are dependent on the calibration phantom is reasonable, because a change in the calibration phantom is reflected in the value of $R_C^{ABS}(\lambda_0)$; therefore, there is only a linear change in $R_P^{REL}(\lambda)$, as defined by Eq. (2).

C. Reflectance as a Function of the Anisotropy Value and the Phase Function

At small source-detector separations, where the diffusion approximation does not apply, the reflectance of light is a function of the absorption coefficient, the scattering coefficient, the phase function of the scattering centers, the boundary conditions and the properties of the source and collection fibers. The phase functions have typically been modeled using either Mie theory [41], the HG approximation [34] or the MHG approximation [9,35]. It has been previously reported that the choice of phase function can have a significant effect on the reflectance of light especially for small source-detector separations [42,43]. When using a monodisperse suspension of spherical particles, the Mie scattering presents very distinguishable oscillations, but as the size distribution increases, the Mie oscillations smooth out [44], and the signal is also masked by a background of diffusely scattered light from the underlying tissue [45]. To determine the influence of the anisotropy value on the reflectance measurements, we decided to use the HG approximation, because it has been commonly used to model the phase function of scattering centers at small source-detector separations [7,8,11,12,14,16,19,21,46,47]. MC simulations were run for a medium with an absorption coefficient of 0.01 cm^{-1} and for a fiber probe tilt angle of 0° and 45°. Fifteen simulations were performed, for each tilt angle, using five different anisotropy values (g = 0.2, 0.5, 0.75, 0.9, and 0.95), and three different reduced scattering coefficient values (μ_s' = 5, 10, and 20 cm^{-1}). The absolute reflectance was determined using Eq. (1). For each reduced scattering coefficient, the percentage variation (PV) of the reflectance referenced to the reflectance with g = 0.9 was calculated using Eq. (7), where $R1$ is the reflectance at a given g value and $R2$ is the reflectance at g = 0.9.

$$\mathrm{PV} = \frac{(R1 - R2)}{R2} \times 100. \tag{7}$$

The PV, for the 0° degree fiber tilt angle, as a function of the anisotropy value for different reduced scattering coefficients is depicted in Fig. 6. Higher reduced scattering coefficient values exhibit lower percentage variation as a function of the g value, compared to lower reduced scattering coefficient values. We note that the percentage variation for all the values of μ_s' is less than 15% for typical biological tissue anisotropy values ($g > 0.75$). Similar results were obtained with the 45° tilt angle.

We repeated the MC simulations described in Subsections 3.A and 3.B to calculate the values of the

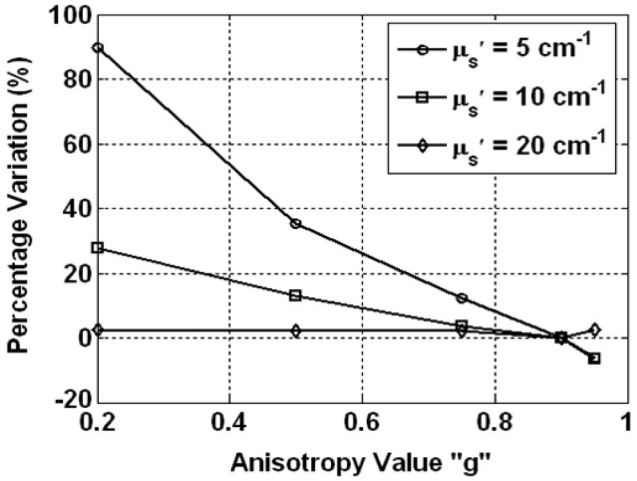

Fig. 6. Percentage variation of the reflectance as a function of the anisotropy value for the 0° fiber probe configuration obtained with Monte Carlo simulations.

coefficients a and a_0 and the mean value of the coefficients b and c with the 0° and 45° fiber probes for the anisotropy values of 0.2, 0.5, 0.75, and 0.95. The results for the anisotropy values of 0.2, 0.5, 0.75, and 0.95 are listed in Table 4 under columns E, F, G, and H, respectively. The values of a_0 and b vary significantly from the results in column A for low g values, and do not depend on the anisotropy value for high g values. For biological tissues we are only interested in high anisotropy values.

To analyze the influence of the phase function on our model, we altered our MC code to model a MHG phase function [9,35]. The angular scatter distribution of the MHG (p_{MHG}) is described by Eq. (8).

$$p_{\mathrm{MHG}}(\theta, g_{\mathrm{HG}}, \xi) = \xi p_{\mathrm{HG}}(\theta, g_{\mathrm{HG}}) + (1-\xi)\frac{3}{4\pi}\cos^2\theta, \tag{8}$$

where g_{HG} and p_{HG} are the anisotropy value and the angular scatter distribution of the HG phase function, respectively, and ξ is a normalization factor. The value of g_{HG} was set to 0.9165 and ξ was set to 0.9, such that the anisotropy value of the MHG was 0.9. Figure 7(a) plots the angular scatter distribution of

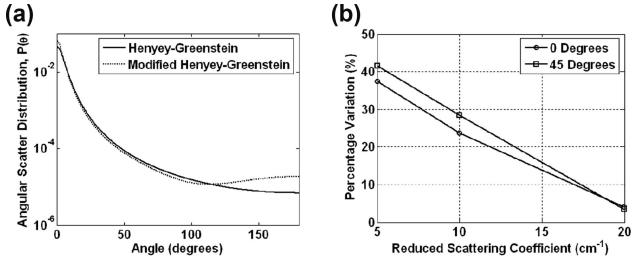

Fig. 7. (a) Angular scatter distribution of the HG and MHG phase function. (b) Percentage variation of the reflectance between the HG and MHG phase function as a function of the reduced scattering coefficient for the 0° and 45° fiber probe configuration obtained with Monte Carlo simulations.

the HG and MHG phase functions where both anisotropy values are equal to 0.9.

We performed MC simulations with the HG and MHG phase function, for the 0° and 45° fiber probe, with a $\mu_s' = 5$, 10, and 20 cm^{-1}; $g = 0.9$; and $\mu_a = 0.01\ \mathrm{cm}^{-1}$. Figure 7(b) shows the PV between the reflectance obtained with the HG and the MHG phase functions, given by Eq. (7) where $R1$ is the reflectance obtained with the MHG and $R2$ is the reflectance obtained with the HG phase function at a given μ_s'. We observe that higher μ_s' values present smaller percentage variation between the two phase functions.

The MC simulations described in Subsections 3.A and 3.B were repeated with the MHG phase function for the 0° and 45° fiber probe. The values of the coefficients a and a_0 and the mean value of the coefficients b and c are listed in Table 4 under column D. Only the value of a_0 appears to vary significantly from the results presented in column A.

D. Extraction of the Optical Properties of a Tissue Model from Monte Carlo Simulations

To validate the model described by Eq. (6), the optical properties of a scattering and absorbing medium were extracted from the reflectance obtained from MC simulations (Subsection 3.D) and from experiments in tissue phantoms (Subsection 3.E). The value of a_0 is dependent on both the phase function and anisotropy value, as described in Subsection 3.C.

The phase function and anisotropy value of the scattering centers are wavelength dependent, and are typically unknown in biological tissue; therefore, to simplify the use of the model described in Eq. (6), we set the value of a_0 to 0.

Two absolute reflectance spectra were generated with MC simulations using the 45° fiber probe. Both spectra have the same reduced scattering coefficient, but different absorption coefficient values, which will be referred to as Lowμ_a and Highμ_a spectra. The wavelengths were selected for the range between 500 and 750 nm in 10 nm steps. The reduced scattering coefficient was modeled using Eq. (9):

$$\mu_s'(\lambda) = d\lambda^{-e}. \tag{9}$$

The value of the exponent e was set to 1.1, based on typical values found in biological tissue [48], and the value of d was selected such that μ_s' (610 nm) = 10 cm^{-1}. The anisotropy value was held constant at 0.9 for all wavelengths. The absorption coefficient was represented by Eq. (10):

$$\mu_a(\lambda) = f_1(f_2\varepsilon_{HbO}(\lambda) + (1-f_2)\varepsilon_{Hb}(\lambda)), \tag{10}$$

where $\varepsilon_{HbO}(\lambda)$ and $\varepsilon_{Hb}(\lambda)$ are the extinction coefficients of oxyhemoglobin and deoxyhemoglobin, respectively. The values of f_1 were selected such that μ_a (610 nm) = 0.2 cm^{-1} for the Lowμ_a spectrum, and μ_a (610 nm) = 1 cm^{-1} for the Highμ_a spectrum. The value of f_2, which represents the oxygen saturation, was set to 0.8.

To extract the optical properties from the MC simulation, Eq. (6) was fitted to the absolute reflectance spectrum, for which the values of a, b, and c were obtained from Tables 1, 2, and 3, respectively; d, e, f_1, and f_2 were the fitting parameters; and a_0 was set to 0. The parameters were bounded as $0 \leq d, e, f_1$ and $0 \leq f_2 \leq 1$.

Figure 8(a) shows the absolute reflectance spectrum and the least square fit to the model, for the Lowμ_a and Highμ_a spectra. The actual and extracted wavelength-dependent reduced scattering coefficients are shown in Fig. 8(b), and the actual and extracted wavelength-dependent absorption coefficients are shown in Fig. 8(c). The values of hemoglo-

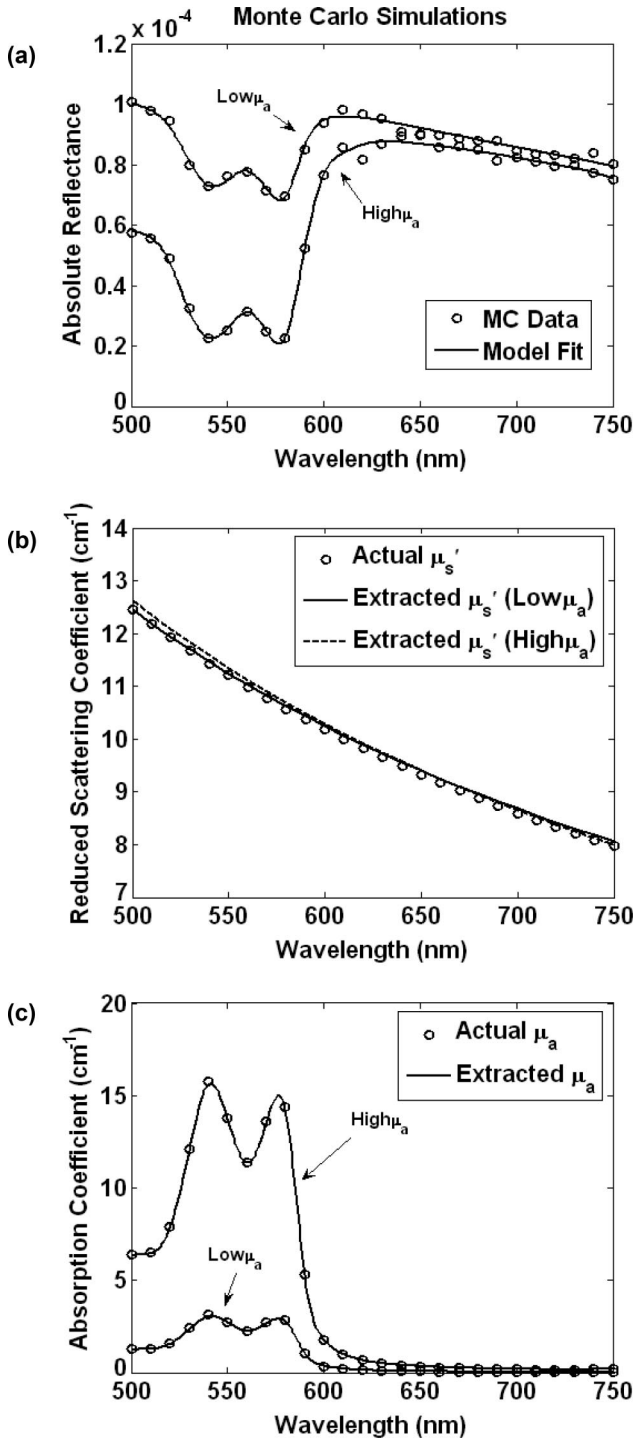

Fig. 8. (a) Absolute reflectance spectrum and model fit for a Monte Carlo simulation with a 45° fiber probe configuration. Actual and extracted (b) reduced scattering coefficient and (c) absorption coefficient.

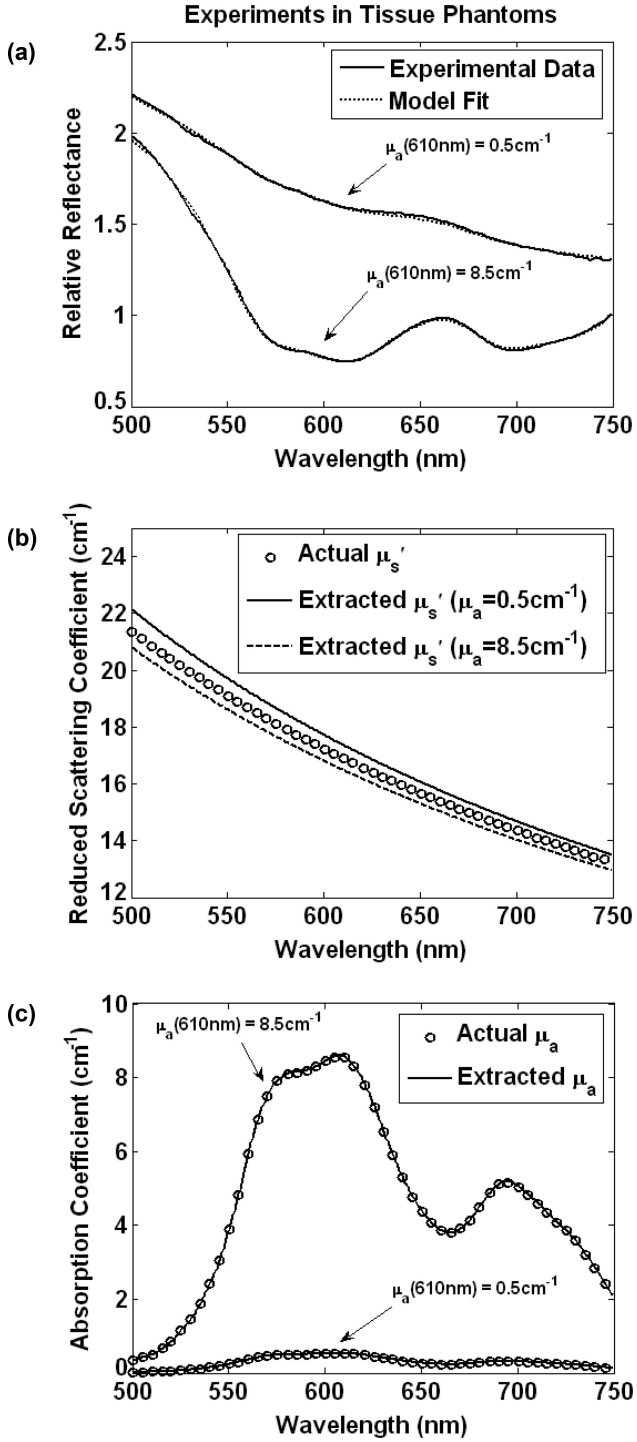

Fig. 9. (a) Relative reflectance spectrum and model fit for experiments in tissue phantoms with a 45° fiber probe configuration. Actual and extracted (b) reduced scattering coefficient and (c) absorption coefficient.

Table 5. Mean and Standard Deviation Over 15 Measurements of the Absorption Coefficient Extracted From Experiments in Tissue Phantoms with a 0°, 15°, 30°, and 45° Fiber Probe Configuration at 610 nm[a]

		Fiber Tilt Angle			
Actual μ_a	Actual μ_s'	0°	15°	30°	45°
0	9.2	0.00 ± 0.00	0.00 ± 0.00	0.00 ± 0.00	0.00 ± 0.00
	17.5	0.00 ± 0.00	0.00 ± 0.00	0.00 ± 0.00	0.00 ± 0.00
0.5	9.2	0.58 ± 0.03	0.58 ± 0.01	0.49 ± 0.00	0.58 ± 0.02
	17.5	0.58 ± 0.02	0.58 ± 0.02	0.49 ± 0.02	0.53 ± 0.02
2.8	9.2	2.71 ± 0.04	3.18 ± 0.03	2.62 ± 0.02	2.89 ± 0.04
	17.5	2.70 ± 0.04	3.10 ± 0.02	2.45 ± 0.14	2.82 ± 0.03
8.5	9.2	7.98 ± 0.14	8.75 ± 0.12	8.01 ± 0.16	8.53 ± 0.19
	17.5	8.39 ± 0.06	8.56 ± 0.52	8.23 ± 0.05	8.57 ± 0.08

[a]Units are in cm^{-1}.

bin oxygen saturation (f_2) obtained were 0.826 and 0.836 for the Lowμ_a and Highμ_a, respectively.

E. Extraction of the Optical Properties of a Tissue Phantom

Eight liquid tissue phantoms were prepared with different optical properties. Two reduced scattering coefficients were used, such that μ_s' (610 nm) was 9.2 and 17.5 cm^{-1}, and four absorption coefficients were used such that μ_a (610 nm) was 0, 0.5, 2.8, and 8.5 cm^{-1}. Measurements were taken with the four fiber probe configurations.

Using Eq. (3), the values of a obtained in Table 1 and the determined values of the reduced scattering coefficient of the calibration phantom μ_{sC}', it was possible to determine theoretically the relative reflectance of the calibration phantom $[R_C^{REL}(\lambda) = R_C^{ABS}(\lambda)/R_C^{ABS}(\lambda_0) = a\mu_{sC}'(\lambda) + a_0]$ when the absorption coefficient is negligible. Because we do not know the wavelength-dependent phase function and anisotropy value of the calibration phantom, we simplify the use of the model by setting the value of a_0 to 0. The incident light at a given wavelength is not necessarily equal to $I_0(\lambda_0)$; therefore, the relative reflectance of the tissue phantom as a function of wavelength $[R_P^{REL}(\lambda)]$, can be calculated with Eq. (11).

$$\begin{aligned} R_P^{REL}(\lambda) &= \frac{R_P^{ABS}(\lambda)}{R_C^{ABS}(\lambda_0)} \\ &= \frac{R_P^{ABS}(\lambda)}{R_C^{ABS}(\lambda_0)} \frac{R_C^{ABS}(\lambda_0)}{R_C^{ABS}(\lambda)} \frac{R_C^{ABS}(\lambda)}{R_C^{ABS}(\lambda_0)} \\ &= \frac{R_P^{ABS}(\lambda)}{R_C^{ABS}(\lambda)} R_C^{REL}(\lambda) \\ &= \frac{I_P(\lambda)}{I_0(\lambda)} \frac{I_0(\lambda)}{I_C(\lambda)} a\mu_{sC}'(\lambda) \\ &= \frac{I_P(\lambda)}{I_C(\lambda)} a\mu_{sC}'(\lambda), \end{aligned} \tag{11}$$

where $I_P(\lambda)$ is the collected light obtained from the tissue phantom and $I_C(\lambda)$ is the collected light obtained from the calibration phantom.

Equation (6) was then fitted to $R_P^{REL}(\lambda)$ for the wavelengths of 500–750 nm. The reduced scattering coefficient was modeled by Eq. (9) and the absorption coefficient was modeled with Eq. (12):

$$\mu_a(\lambda) = f_1 \varepsilon_{dye}(\lambda), \tag{12}$$

where $\varepsilon_{dye}(\lambda)$ is the extinction coefficient of the Indigo Blue dye. The fitting coefficients were bounded by $0 \le d, e, f_1$; the values of a, b, and c were obtained from Tables 1, 2, and 3, respectively; and a_0 was set to 0. Figure 9(a) shows the relative reflectance spectrum and the least square fit to the model, using the 45° fiber optic probe configuration, for μ_s' (610 nm) = 17.5 cm^{-1} and μ_a (610 nm) = 0.5 and 8.5 cm^{-1}. The actual and extracted wavelength-dependent reduced scattering coefficients are shown in Fig. 9(b), and the actual and extracted wavelength-dependent absorption coefficients are shown in Fig. 9(c).

Tables 5 and 6 present the mean and standard deviation values of the absorption and reduced scattering coefficients over 15 measurements determined with all the fiber probe configurations in the eight phantoms at 610 nm, respectively. The errors in estimating the absorption and scattering coefficients between the mean μ_a and actual μ_a was less than

Table 6. Mean and Standard Deviation Over 15 Measurements of the Reduced Scattering Coefficient Extracted From Experiments in Tissue Phantoms With a 0°, 15°, 30°, and 45° Fiber Probe Configuration at 610 nm[a]

Actual	Actual	Fiber Tilt Angle			
μ_s'	μ_a	0°	15°	30°	45°
9.2	0	8.7 ± 0.3	8.8 ± 0.1	9.1 ± 0.1	9.6 ± 0.1
	0.5	9.0 ± 0.3	9.6 ± 0.1	9.0 ± 0.1	9.1 ± 0.2
	2.8	8.5 ± 0.3	9.5 ± 0.2	9.7 ± 0.0	9.2 ± 0.3
	8.5	9.3 ± 0.3	9.6 ± 0.2	9.3 ± 0.1	8.8 ± 0.3
17.5	0	16.9 ± 1.1	17.4 ± 0.5	17.4 ± 0.2	18.3 ± 0.6
	0.5	17.4 ± 0.9	19.0 ± 1.0	17.3 ± 0.2	17.3 ± 0.9
	2.8	16.4 ± 0.7	18.4 ± 0.4	17.6 ± 1.1	18.3 ± 0.4
	8.5	18.5 ± 0.4	17.1 ± 2.0	17.2 ± 0.2	16.4 ± 0.4

[a]Units are in cm^{-1}.

20% and between the mean μ_s' and actual μ_s was less than 10%.

The analysis was also performed by using a calibration phantom prepared with Intralipid and deionized water, which has different optical properties than that of a titanium dioxide suspension. The errors in estimating μ_a and μ_s' were slightly reduced; however, the disadvantage of using Intralipid as a calibration phantom is that its optical properties can change with time as the solution degrades.

4. Discussion and Conclusions

A simple analytical model for describing the reflectance of a scattering and absorbing medium has been presented. The model is successful in describing the reflectance spectrum at small source-detector separations and is not limited to a parameter range with scattering much larger than absorption, a limitation that generally plagues models based on diffusion theory.

MC simulations indicate that tilting both the source and the detector optical fibers, such that the fibers are parallel to each other, enhances the sensitivity to superficial volumes of tissue, while maintaining a fiber-probe geometry that is convenient for clinical applications and is easy to fabricate. Further studies will assess the depth of penetration of the photons as a function of the tissue optical properties and fiber tilt angle. The model has been shown to work well for fiber probe tilt angles between 0° and 45°.

The model has been defined by Eq. (6), and the coefficients a, a_0, b, and c have been listed in Tables 1, 2, and 3. The value of the coefficient a differs between the MC simulations and the experiments in tissue phantoms because the former measures absolute reflectance while the latter measures relative reflectance. The values of a and a_0 depend on the optical properties of the calibration phantom. If a calibration phantom with different optical properties is used, new values for a and a_0 should be determined experimentally as described in Subsection 3.A. A change in the optical properties of a calibration phantom is reflected in the value $R_C^{ABS}(\lambda_0)$, which translates to a linear change of $R_P^{REL}(\lambda)$, as defined by Eq. (2). Therefore, only the values of a and a_0 are affected by the details of the calibration phantom, while the values of b and c remain the same, as it was demonstrated by comparing the results of using a calibration phantom made with Intralipid instead of titanium dioxide. Although any wavelength of the calibration phantom could be used as a reference, in this study the value of 610 nm was chosen, because it matches the absorption peak of the Indigo Blue dye.

Typically, reflectance measurements are calibrated by dividing the tissue spectral measurement by a spectrum measured with a spectrally-flat diffuse-reflector reference material instead of a calibration phantom measurement as described in this paper. The advantages of using an immersion-type liquid calibration phantom as a reference, as described in this paper, are:

(1) When using a diffuse reflector, the distance between the fiber probe and the reflector surface must be fixed and repeatable if absolute values for optical properties are sought, as opposed to submerging the fiber probe in the liquid calibration phantom, which minimizes the possibility of error and is easily repeatable.

(2) A fiber probe with tips faceted at 45° exhibits total internal reflection when the fiber tip is in air; however, most of the light emerges when the fiber tip is in contact with water (or tissue).

The model for the mean average pathlength expressed by Eq. (5) was determined intuitively and verified empirically. Although an analytical derivation for the mean average path length is not provided, it has been shown in this paper that Eq. (5) enables successful modeling of the reflectance spectrum of a turbid medium with remarkable accuracy, when it is incorporated in the model defined by Eq. (6).

For a given tilt-angle fiber probe, the values of the coefficients b and c agree well for different values of μ_a and μ_s', which validates the model, as observed in Tables 2 and 3. The value of c is determined to be between 0.19 and 0.21 by both the MC simulations and the experimental results; however, there is disagreement for the value of b. Although we have not uniquely determined the source for that discrepancy, we note that it is consistent with the fact that the center-to-center fiber separation of the fiber probes fabricated were approximately 238 μm, instead of 250 μm as used in the simulations. Table 4 indicates that the value of b depends on the fiber separation, as observed when comparing b values obtained with probes that have a separation of 200 and 250 μm. The value of b increases for smaller anisotropy values but the experimental tissue phantoms are highly forward scattering; therefore, we do not attribute the variation of b to small anisotropy values.

Based on MC simulations and the results presented in Table 4, we can determine that the coefficients of the model do not depend on the indices of refraction of the fiber and the medium, and if the same phase function is used, the coefficients are not affected for different values of highly forward scattering anisotropies. However, the coefficient a_0 is affected by the phase function and by low anisotropy values.

At small source-detector separations, the reflectance spectrum is dependent on the details of the phase function and the anisotropy value of the scattering centers. The reflectance was calculated for different anisotropy values using the HG approximation and was also calculated using a MHG phase functions with an anisotropy value of 0.9. It was determined that the reflectance is sensitive to the anisotropy value and phase function for low-scattering coefficients, but relatively insensitive for high scattering coefficients, where the photons undergo more

scattering events before being collected, which allows the photons to lose track of their original directions. This effect can be observed in Figs. 6 and 7(b). It was also determined that for anisotropy values typically found in tissue ($g > 0.75$), the reflectance varies less than 15% for all values of μ_s'.

The model was tested by reconstructing the optical properties of a spectral reflectance obtained from MC simulations. The extracted values for the reduced scattering and absorption coefficients agree well with the actual values [Figs. 8(b) and 8(c)]. The values of the hemoglobin oxygen saturation extracted were also close to the actual values. This validates the inversion algorithm with an approach that can be used *in vivo* in biological tissue with typical values of optical properties.

The model was tested in tissue phantoms, and the values of the extracted optical properties agree well with the actual values (Tables 5 and 6). The errors for the absorption coefficient were less than 20%, while the errors for the reduced scattering coefficient were less than 10%. Equation (11) depends on $R_C^{REL}(\lambda)$, which is calculated theoretically by setting $a_0 = 0$. The data was reanalyzed by using a calibration phantom made from Intralipid, for which the results were slightly improved, indicating that the real values of a_0 in Intralipid, for all wavelengths, are closer to 0 than is the case for a suspension of titanium dioxide. The disadvantage of using Intralipid as a calibration phantom is that its optical properties are less stable over time.

The phase function and anisotropy value of real tissue is not well-defined and is wavelength dependent; therefore, the specific value of a_0 would be unknown. By setting a_0 to 0 we are assuming that the effect of the phase function of the scattering centers is small throughout the model; hence, the model is a simplification of light transport in a turbid medium. Further studies will asses the validity of the model for a wide range of phase functions and anisotropy values typically found in tissues. Nevertheless, we were able to reconstruct the reduced scattering and absorption coefficients with good accuracy.

The model is applicable for fiber probe configurations with various tilt angles, for the geometry depicted in this paper. Fiber probes with this geometry are compatible with endoscope channels, which will allow measurements in tissues such as the colon and esophagus. The model has been empirically derived and validated using both MC simulations and experiments in tissue phantoms.

The authors acknowledge support from the National Institutes of Health (NIH) fellowship F31CA119916, NIH grant U54 CA104677, and the Boston University Photonics Center.

References

1. I. J. Bigio and J. R. Mourant, "Ultraviolet and visible spectroscopies for tissue diagnostics: fluorescence spectroscopy and elastic-scattering spectroscopy," Phys. Med. Biol. **42,** 803–814 (1997).
2. O. A'Amar, R. D. Ley, and I. J. Bigio, "Comparison between ultraviolet-visible and near-infrared elastic scattering spectroscopy of chemically induced melanomas in an animal model," J. Biomed. Opt. **9,** 1320–1326 (2004).
3. I. J. Bigio and S. G. Bown, "Spectroscopic sensing of cancer and cancer chemotherapy, current status of translational research," CancerBiol. Ther. **3,** 259–267 (2004).
4. T. J. Farrell, M. S. Patterson, and B. C. Wilson, "A diffusion theory model of spatially resolved, steady-state diffuse reflectance for the non-invasive determination of tissue optical properties *in vivo*," Med. Phys. **19,** 879–888 (1992).
5. A. Kienle and M. S. Patterson, "Improved solutions of the steady-state and the time-resolved diffusion equations for reflectance from a semi-infinite turbid medium," J. Opt. Soc. Am. A **14,** 246–254 (1997).
6. R. M. P. Doornbos, R. Lang, M. C. Aalders, F. W. Cross, and H. J. C. M. Sterenborg, "The determination of *in vivo* human tissue optical properties and absolute chromophore concentrations using spatially resolved steady-state diffuse reflectance spectroscopy," Phys. Med. Biol. **44,** 967–981 (1991).
7. G. Zonios and A. Dimou, "Modeling diffuse reflectance from semi-infinite turbid media: application to the study of skin optical properties," Opt. Express **14,** 8661–8674 (2006).
8. M. Johns, C. A. Giller, D. C. German, and H. Liu, "Determination of reduced scattering coefficient of biological tissue from a needle-like probe," Opt. Express **13,** 4828–4842 (2005).
9. F. Bevilacqua and C. Depeursinge, "Monte Carlo study of diffuse reflectance at source-detector separations close to one transport mean free path," J. Opt. Soc. Am. A **16,** 2935–2945 (1999).
10. A. Amelink, H. J. C. M. Sterenborg, M. P. L. Bard, and S. A. Burgers, "*In vivo* measurement of the optical properties of tissue by use of differential path-length spectroscopy," Opt. Lett. **29,** 1087–1089 (2004).
11. A. Amelink and H. J. C. M. Sterenborg, "Measurement of the local optical properties of turbid media by differential path-length spectroscopy," Appl. Opt. **43,** 3048–3054 (2004).
12. T. P. Moffitt and S. A. Prahl, "Sized-fiber reflectometry for measuring local optical properties," IEEE J. Sel. Top. Quantum Electron. **7,** 952–958 (2001).
13. F. Bevilacqua, D. Piguet, P. Marquet, J. D. Gross, B. J. Tromberg, and C. Depeursinge, "*In vivo* local determination of tissue optical properties: applications to human brain," Appl. Opt. **38,** 4939–4950 (1999).
14. C. K. Hayakawa, J. Spanier, F. Bevilacqua, A. K. Dunn, J. S. You, B. J. Tromberg, and V. Venugopalan, "Perturbation Monte Carlo methods to solve inverse photon migration problems in heterogeneous tissues," Opt. Lett. **26,** 1335–1337 (2001).
15. C. K. Hayakawa, B. Y. Hill, J. S. You, F. Bevilacqua, J. Spanier, and V. Venugopalan, "Use of the delta-P1 approximation for recovery of optical absorption, scattering, and asymmetry coefficients in turbid media," Appl. Opt. **43,** 4677–4684 (2004).
16. Q. Liu and N. Ramanujam, "Sequential estimation of optical properties of a two-layered epithelial tissue model from depth-resolved ultraviolet-visible diffuse reflectance spectra," Appl. Opt. **45,** 4776–4790 (2006).
17. G. M. Palmer and N. Ramanujam, "A Monte Carlo based inverse model for calculating tissue optical properties, part I: theory and validation on synthetic phantoms," Appl. Opt. **45,** 1062–1071 (2006).
18. G. M. Palmer, C. Zhu, T. M. Breslin, F. Xu, K. W. Gilchrist, and N. Ramanujam, "A Monte Carlo based inverse model for calculating tissue optical properties, part II: application to breast cancer diagnosis," Appl. Opt. **45,** 1072–1078 (2006).
19. T. J. Pfefer, L. S. Matchette, C. L. Bennett, J. A. Gall, J. N. Wilke, A. Durkin, and M. N. Ediger, "Reflectance-based deter-

mination of optical properties in highly attenuating tissue," J. Biomed. Opt. **8,** 206–215 (2003).
20. G. Zonios, L. T. Perelman, V. Backman, R. Manoharan, M. Fitzmaurice, J. Van Dam, and M. S. Feld, "Diffuse reflectance spectroscopy of human adenomatous colon polyps *in vivo*," Appl. Opt. **38,** 6628–6637 (1999).
21. J. Sun, K. Fu, A. Wang, A. W. H. Lin, U. Utzinger, and R. Drezek, "Influence of fiber optic probe geometry on the applicability of inverse models of tissue reflectance spectroscopy: computational models and experimental measurements," Appl. Opt. **45,** 8152–8162 (2006).
22. U. Utzinger and R. Richards-Kortum, "Fiber optic probes for biomedical optical spectroscopy," J. Biomed. Opt. **8,** 121–147 (2003).
23. A. Myakov, L. Nieman, L. Wicky, U. Utzinger, R. Richards-Kortum, and K. Sokolov, "Fiber optic probe for polarized reflectance spectroscopy *in vivo*: design and performance," J. Biomed. Opt. **7,** 388–397 (2002).
24. C. Xhu, Q. Liu, and N. Ramanujam, "Effect of fiber optic probe geometry on depth-resolved fluorescence measurements from epithelial tissues: a Monte Carlo simulation," J. Biomed. Opt. **8,** 237–247 (2003).
25. T. J. Pfefer, K. T. Schomacker, M. N. Ediger, and N. S. Nishioka, "Multiple-fiber probe design for fluorescence spectroscopy in tissue," Appl. Opt. **41,** 4712–4721 (2002).
26. A. Wang, J. Bender, U. Utzinger, and R. Drezek, "Depth-sensitive reflectance measurements using obliquely oriented fiber probes," J. Biomed. Opt. **10,** 044017 (2005).
27. L. Nieman, A. Myakov, J. Aaron, and K. Sokolov, "Optical sectioning using a fiber probe with an angled illumination-collection geometry: evaluation in engineered tissue phantoms," Appl. Opt. **43,** 1308–1319 (2004).
28. J. Pfefer, A. Agrawal, and R. Drezek, "Oblique-incidence illumination and collection for depth-selective fluorescence spectroscopy," J. Biomed. Opt. **10,** 044016 (2005).
29. S. P. Lin, L. Wang, S. L. Jacques, and F. K. Tittel, "Measurement of tissue optical properties by the use of oblique-incidence optical fiber reflectometry," Appl. Opt. **36,** 136–143 (1997).
30. D. Arifler, R. A. Schwarz, S. K. Chang, and R. Richards-Kortum, "Reflectance spectroscopy for diagnosis of epithelial precancer: model-based analysis of fiber-optic probe designs to resolve spectral information from epithelium and stroma," Appl. Opt. **44,** 4291–4305 (2005).
31. S. L. Jacques and L. Wang, "Monte Carlo modeling of light transport in tissue," in *Optical-Thermal Response of Laser Irradiated Tissue,* A. J. Welch and M. J. C. van Gemert, eds. (Plenum, 1995), pp. 73–100.
32. L. H. Wang, S. L. Jacques, and L. Zheng, "MCML: Monte-Carlo modeling of light transport in multilayered tissues," Comput. Methods Programs Biomed. **47,** 131–146 (1995).
33. M. Hiraoka, M. Firbank, M. Essenpreis, M. Cope, S. R. Arridge, P. van der Zee, and D. T. Delpy, "A Monte Carlo investigation of optical pathlength in inhomogeneous tissue and its application to near-infrared spectroscopy," Phys. Med. Biol. **38,** 1859–1876 (1993).
34. L. G. Henyey and J. L. Greenstein, "Diffuse radiation in the galaxy," Astrophys. J. **93,** 70–83 (1941).
35. P. Thueler, I. Charvet, F. Bevilacqua, M. St. Ghislain, G. Ory, P. Marquet, P. Meda, B. Vermeulen, and C. Depeursinge, "*In vivo* endoscopic tissue diagnostics based on spectroscopic absorption, scattering and phase function properties," J. Biomed. Opt. **8,** 495–503 (2003).
36. S. T. Flock, S. L. Jacques, B. C. Wilson, W. M. Star, and M. J. C. van Germet, "Optical properties of Intralipid: a phantom medium for light propagation studies," Lasers Surg. Med. **12,** 510–519 (1992).
37. M. G. Nichols, E. L. Hull, and T. H. Foster, "Design and testing of a white-light, steady-state diffuse reflectance spectrometer for determination of optical properties of highly scattering systems," Appl. Opt. **36,** 93–104 (1997).
38. M. Firbank and D. T. Delpy, "A design for a stable and reproducible phantom for use in near infra-red imaging and spectroscopy," Phys. Med. Biol. **38,** 847–853 (1993).
39. W. F. Cheong, S. A. Prahl, and A. J. Welch, "A review of the optical properties of biological tissues," IEEE J. Quantum Electron. **26,** 2166–2185 (1990).
40. A. Sassaroli and S. Fantini, "Comment on the modified Beer–Lambert law for scattering media," Phys. Med. Biol. **49,** N255–N257 (2004).
41. C. F. Bohren and D. R. Huffman, *Absorption and Scattering of Light by Small Particles* (Wiley, 1983).
42. J. R. Mourant, J. Boyer, A. H. Hielscher, and I. J. Bigio, "Influence of the phase function on light transport measurements in turbid media performed with small source-detector separations," Opt. Lett. **21,** 546–548 (1996).
43. M. Canpolat and J. R. Mourant, "High-angle scattering events strongly affect light collection in clinically relevant measurement geometries for light transport through tissue," Phys. Med. Biol. **45,** 1127–1140 (2000).
44. M. Canpolat and J. R. Mourant, "Particle size analysis of turbid media with a single optical fiber in contact with the medium to deliver and detect white light," Appl. Opt. **40,** 3792–3799 (2001).
45. L. T. Perelman, V. Backman, M. Wallace, G. Zonios, R. Manoharan, A. Nusrat, S. Shields, M. Seiler, C. Lima, T. Hamano, I. Itzkan, J. Van Dam, J. M. Crawford, and M. S. Feld, "Observation of periodic fine structure in reflectance from biological tissue: a new technique for measuring nuclear size distribution," Phys. Rev. Lett. **80,** 627–630 (1998).
46. A. Dunn and D. Boas, "Transport-based image reconstruction in turbid media with small source-detector separations," Opt. Lett. **25,** 1777–1779 (2000).
47. P. R. Bargo, S. A. Prahl, and S. L. Jacques, "Collection efficiency of single optical fiber in turbid media," Appl. Opt. **42,** 3187–3197 (2003).
48. J. R. Mourant, J. P. Freyer, A. H. Hielscher, A. A. Eick, D. Shen, and T. M. Johnson, "Mechanisms of light scattering from biological cells relevant to noninvasive optical-tissue diagnostics," Appl. Opt. **37,** 3586–3593 (1998).